Controlling Defect Chemistry in InTe by Saturation Annealing

Shantanu Misra, Petr Levinský, Jiří Hejtmánek, Christophe Candolfi, Bertrand Lenoir

To cite this version:

Shantanu Misra, Petr Levinský, Jiří Hejtmánek, Christophe Candolfi, Bertrand Lenoir. Controlling Defect Chemistry in InTe by Saturation Annealing. ACS Applied Energy Materials, 2022, 5 (11), pp.13714-13722. 10.1021/acsaem.2c02364 . hal-03969497

HAL Id: hal-03969497
https://hal.univ-lorraine.fr/hal-03969497v1

Controlling defect chemistry in InTe by saturation annealing

Shantanu Misra[1], Petr Levinský[2], Jiří Hejtmánek[2], Christophe Candolfi[1,*], Bertrand Lenoir[1,*]

[1] *Institut Jean Lamour, UMR 7198 CNRS – Université de Lorraine, Campus ARTEM, 2 allée André Guinier, BP 50840, 54011 Nancy, France*

[2] *FZU – Institute of Physics of the Czech Academy of Sciences, Cukrovarnická 10/112, 162 00, Prague 6, Czech Republic*

ABSTRACT

Achieving a precise control of defects in chalcogenide semiconductors is paramount to optimizing their thermoelectric properties. Recently, *p*-type InTe has emerged as a potential candidate for thermoelectric applications in power generation, mainly due to its extremely low lattice thermal conductivity. Here, we show that the concentration of inherent In vacancies in both single-crystalline and polycrystalline InTe samples can be successfully controlled through saturation annealing. This process, performed on both the In-rich and Te-rich sides of the solidus line at 943, 893, 843 K and 943 K, respectively, results in variations in the hole concentration from 4.9×10^{19} to 8.5×10^{19} cm^{-3} at 300 K. This narrow density range suggests that the defect chemistry in InTe plays a less critical role in determining its thermoelectric properties compared to other state-of-the-art thermoelectric chalcogenides. The increased partially-degenerate character of transport with increasing the annealing temperature lowers the thermoelectric performance, with a peak ZT value of 0.9 achieved at 800 K in as-synthesized InTe.

KEYWORDS: *thermoelectric, chalcogenide, defects, saturation annealing, semiconductors*

1. INTRODUCTION

Thermoelectric energy harvesting provides a versatile way for directly converting waste heat into electrical energy or vice versa. The conversion efficiency of a thermoelectric material is determined by its dimensionless thermoelectric figure of merit ZT defined as $ZT = \alpha^2 T / \rho(\kappa_e + \kappa_{ph})$ where α is the Seebeck coefficient (or thermopower), ρ is the electrical resistivity, T is the absolute temperature and κ_e and κ_{ph} are the electronic and lattice thermal conductivity, respectively.[1-3] Effective strategies to optimize the ZT values center upon either increasing the power factor α^2 / ρ through band-structure engineering (band convergence, resonant levels or introduction of magnetic ions)[4-15] or lowering the heat propagation. This last strategy can be realized in materials with high intrinsic anharmonicity or by using specific synthesis techniques to modify the microstructure from the nano to the microscale.[16-22]

Over the last decades, chalcogenide semiconductors have stood as the best candidates for mid-temperature-range (500 – 800 K) thermoelectric applications in power generation.[23-31] Most of the best-performing chalcogenides exhibit deviations from their ideal stoichiometry, with vacancies and antisite defects being the main type of intrinsic defects.[1,2] Because both of them can strongly alter the electronic and thermal properties, controlling their concentration is a central aspect to effectively design high-performance thermoelectric materials. As robust approaches for controlling the chemical composition of chalcogenides, phase boundary mapping and saturation annealing have been applied to several thermoelectric materials including $CoSb_3$,[32] the Zintl phases $Ca_9Zn_{4+x}Sb_9$ and Mg_3Sb_2,[33,34] GeTe,[35] PbX (X = S, Se, Te),[36-39] Bi_2Te_3 (Refs. 40 and 41), SnX (X = S, Se, Te).[42-45] The former strategy relies on a systematic investigation of the phase diagram around the targeted composition by probing all distinct multiphase equilibria to access the full range of thermodynamically-allowed defect concentrations. However, an unavoidable drawback of this technique is the presence of small concentrations of one of several secondary phases that can affect the carrier mobility and trigger instabilities upon thermal cycling. Saturation annealing enables to circumvent this issue by investigating the maximum deviations from the ideal stoichiometry at a fixed temperature on every side of the solidus line.[35-45] Furthermore, this synthesis process, performed under strict thermodynamic equilibrium conditions, yields reproducible results from sample to sample, prepared in both single-crystalline and polycrystalline forms.

Here, we show that this technique can be also applied to single-crystalline and polycrystalline InTe, a chalcogenide semiconductor that has recently emerged as an interesting thermoelectric material due to its extremely low lattice thermal conductivity.[46-60] This process, realized on both the In-rich and Te-rich sides of the solidus line at selected temperatures varying between 843 and 943 K, results in hole densities ranging from 4.9×10^{19} up to 8.5×10^{19} cm^{-3} at 300 K. While the results obtained on the In-rich side are consistent with the presence of a small amount of singly-charged, acceptor-like In vacancies, the lower hole density achieved for the sample annealed on the Te-rich side suggests the formation of donor-like defects that partially compensate holes.[46,57] In spite of the narrow hole concentration range accessible, the low-temperature transport properties markedly vary with the annealing temperature. The ZT values of all saturated samples, that range between 0.7 and 0.8 around 770 K, are slightly lower than the peak ZT achieved in as-synthesized InTe (0.9 at 710 K) due to their increased degenerate character.

2. RESULTS AND DISCUSSION

The PXRD patterns show that the non-annealed and saturation-annealed samples (see Supporting Information for experimental details and Figure S1 for a photograph of the experimental procedure of the saturation-annealing technique) on the In-rich side are phase pure

(Figure 1) within the detection limit of this technique. All the reflections are indexed by the tetragonal crystal structure of InTe (space group *I*4/*mcm*, No. 140).[49,60] In contrast, the sample annealed on the Te-rich side showed additional reflections at 2θ~25° and 2θ~42°, indicating the precipitation of a secondary phase. These two peaks may correspond to the two main reflections of the cubic In_2Te_3 phase (space group $F\bar{4}3m$, No. 216).[61] Hereafter, the as-synthesized sample will be labelled as InTe, the samples saturation-annealed on the In-rich side at 943, 893 and 843 K will be referred to as In943, In893 and In843, respectively, and the sample saturation-annealed at 943 K on the Te-rich side will be labelled Te943. In agreement with XRD, SEM analyses did not reveal the presence of secondary phases in InTe and in the In943, In893 and In843 samples. Regardless of the annealing temperature, elemental X-ray maps (Figure S2 in SI) further evidenced a homogeneous spatial distribution of In and Te. For the Te943 sample, the presence of small regions of a Te-rich phase evidenced by PXRD was confirmed. This difference between the In-rich and Te-rich sides suggests that the shape of the homogeneity range in the vicinity of the stoichiometric composition InTe is not symmetric, with a possible decrease in the solubility of Te with decreasing temperature on the Te-rich side of the phase diagram. Such a retrograde solubility, observed in Sb_2Te_3 and GeTe,[62,63] may explain the internal precipitation of Te, being removed from the lattice during the quenching process and leading to the formation of a Te-rich secondary phase dispersed in the InTe matrix. The fact that only precipitation of Te is observed suggests that the diffusion coefficient of Te in InTe is significantly higher than that of In, similar to the strong difference between the diffusion of Sn and Te in SnTe.[64,65] This phenomenon is consistent with the lower density of this sample (~91%) after saturation annealing with respect to the samples saturated at the In-rich side, the densities of which have not appreciably changed upon annealing. Thus, the cooling rate applied during quenching is likely fast enough to prevent the sublimation of Te at 943 K but nevertheless too slow to avoid internal precipitation. Note that the quenching rate achieved by using a mixture of water, ice and salt might still be too low to prevent Te precipitation, with the efficiency of the quenching rate in preventing internal precipitation being limited by the specific heat and, most importantly, the very low thermal conductivity of InTe.

All samples display a similar microstructure (Figure S3 in SI), with grains formed by stacked plate-like InTe layers. This layer-like structure originates from the $(In^{3+}Te_4{}^{2})^{-}$ tetrahedra chains weakly bounded to each other that lead to easy cleavage along the (110) plane in single-crystalline InTe.[55,66,67] This characteristic explains the anisotropic transport properties observed in polycrystalline and single-crystalline samples.[46-60]

Figure 2 shows the temperature dependence of the electrical resistivity ρ. Hereafter, because all the samples show only a small degree of anisotropy that remains similar from sample to sample and as a function of temperature, only measurements performed in the direction parallel to the pressing direction, that is, the direction along which the thermoelectric performance is the highest, are shown. Measurements performed along the perpendicular direction on the as-synthesized and saturation-annealed samples can be found in the SI (Figures S4 to S11). The effectiveness of the saturation annealing process is demonstrated by the distinct behaviors in $\rho(T)$. For samples annealed at the In-rich side, $\rho(T)$ exhibits a complex temperature dependence, which contrasts with the simple linear-in-T behavior expected in conventional degenerate systems and observed in single-crystalline InTe.[55] The temperature at which $\rho(T)$ deviates from the linear dependence decreases from 500 K in InTe to around 300 K in the saturation-annealed samples. Below these temperatures where a minimum is reached, $\rho(T)$ shows a thermally-activated behavior mimicking a semiconducting-like dependence. This behavior persists down to 175 K where a shoulder is consistently observed in all samples. Upon further cooling below this temperature, the variations in ρ are strongly lessened with decreasing the annealing temperature. In particular, while the ρ values of the sample annealed at 843 K slightly decrease upon cooling, a pronounced rise in ρ is observed for the sample annealed at

943 K with no sign of saturation down to 5 K. The temperature of the shoulder is consistent with the magnetotransport anomalies observed in single-crystalline InTe and is likely connected to the disordered In^+ cations, residing in the large tunnels of the crystal structure, that undergo a static-to-dynamic crossover between 100 and 200 K.[54] Due to the precipitation of a secondary phase and the lower density of the Te943 sample, its ρ values increase by two orders of magnitude upon cooling. Despite this distinct behavior, the shoulder observed in the samples saturated at the In-rich side is still visible near 175 K.

The distinct trends in $\rho(T)$ and the thermally-activated behavior observed upon cooling below 300 K is likely associated with intrinsic resistance from grain boundaries. This impact of the microstructure on the electrical resistivity, already present in the as-synthesized sample, is strongly lessened in samples saturation-annealed at 893 and 843 K, resulting in a nearly-metallic behavior recovered in the latter. These results are consistent with the metallic-like dependence reported previously in as-grown, single-crystalline InTe and in the single-crystalline sample saturation–annealed at 893 K (Figure S10 in SI) for which grain boundary scattering is absent. The fact that the thermally-activated behavior tends to fade with saturation-annealing may be due to an increase in the average grain size leading to lower electrical resistivity. These results contrast with those reported for SnTe, for which as-synthesized samples show metallic behavior that remains unaffected by annealing treatments,[44] but are similar to those reported for the Zintl compound Mg_3Sb_2 where saturation annealing was shown to suppress grain boundary resistance at low temperatures.[34]

A link between this crossover and the low-temperature shoulder in the $\rho(T)$ data is further supported by the Hall coefficient R_H shown as a function of temperature in Figure 3a. The $R_H(T)$ data of the InTe, In943 and In893 samples are characterized by an anomaly around 175 K, which is also observed in measurements performed perpendicular to the pressing direction (Figure S2 in SI). The fact that this anomaly is not clearly visible for the sample annealed at

843 K is in line with the lessened shoulder in $\rho(T)$. Similar to what has been observed in single-crystalline InTe,[55] this anomaly does not influence the sign of R_H, which remains positive over the entire temperature range, characteristic of a dominant hole-like response.

At 300 K, the hole concentration p_H of 4.5×10^{19} cm^{-3} (Figure 3b and Table 1 where the room-temperature data are gathered) for the as-synthesized InTe sample is in good agreement with the sample prepared by Back *et al*,[58] but comparatively higher than those reported in prior studies.[46-60] p_H hardly evolves with temperature regardless of the annealing temperature, following the trend expected for heavily-doped semiconductors. On the In-rich side, p_H tends to increase with increasing the annealing temperature from 4.9×10^{19} to 8.5×10^{19} cm^{-3} at 300 K for the polycrystalline In843 and In943 samples, respectively. The similar p_H measured in the saturation-annealed and single-crystalline samples (9.5×10^{19} cm^{-3} at 300 K for the single-crystalline sample) indicates that the annealing times applied were sufficient to reach equilibrium at all temperatures. This conclusion is further confirmed by the p_H value similar to within experimental uncertainty measured in a second saturated single-crystalline sample (1.2×10^{20} cm^{-3} at 300 K) that was placed in the same silica tube. Furthermore, these values are similar to those achieved in the two polycrystalline samples, further demonstrating that grain boundaries had little influence on the diffusion process. Note that the direct comparison between the p_H values measured in polycrystalline and single-crystalline samples should be taken with some caution due to the small but discernible anisotropy that exists in the R_H values in both types of samples. Nevertheless, the fact that this anisotropy remains small and constant upon cooling makes the present comparison reasonable.

For the Te943 sample annealed on the Te-rich side, p_H is equal to 5.2×10^{19} cm^{-3} at 300 K, that is, close to the value measured in the as-synthesized sample. Of note, the dispersed Te-rich secondary phase evidenced by SEM is not expected to contribute charge carriers to the matrix. Thus, this value can be considered to correspond to the deviation of stoichiometry at the effective quenching temperature, likely slightly lower than 943 K. The persistent *p*-type character of the samples, which is independent of the annealing temperature and annealing conditions (In- or Te-rich), is consistent with formation energy calculations of native defects in InTe, indicating that vacancies on the In^{1+} site is the dominant defect under both In- and Te-rich annealing conditions.[60] Relatively close in energy are neutral Frenkel defects formed by In vacancies and In intertstitials, the concentration of which is expected to remain low.[57] The presence of a low concentration of In vacancies agrees with the lightly-doped character of all the samples, corresponding to a chemical potential pinned near the top of the valence band manifold and confirmed by low-temperature specific heat measurements.[54] However, the hole count generated by In vacancies is expected to be the highest in the Te-rich side, similar to the case of $Sn_{1-\delta}Te$ where the concentration of Sn vacancies δ is high under such conditions.[42,43] This expectation seems inconsistent with the experimental result that the hole concentration of the as-synthesized and annealed samples are relatively similar. This contradiction might be explained by the formation of donor-like defects partially compensating holes provided by the In vacancies. Similar contradiction between experiments and theoretical predictions of native point defects has notably been underlined in PbTe for which the accurate determination of the position of the valence and conduction band edges and the inclusion of spin-orbit coupling were found to be essential in reproducing the experimental trends.[68] The fact that the band gap of InTe experimentally observed has not been reproduced so far by calculations might explain the present discrepancy between theory and experiment.

Combining all these data, a hypothetical solidus line was drawn (dashed line in Figure 3c), with the possible retrograde solubility of Te highlighted on the left-hand side of the plot. This portion of the diagram is qualitatively similar to that determined for Sb_2Te_3,[62] but with a significantly narrower hole concentration window experimentally accessible in InTe.

The Hall mobility μ_H increases with decreasing the annealing temperature by one order of magnitude below 175 K (Figure 3d and Figure S11 in SI) from 2 cm^2 V^{-1} s^{-1} to 20 cm^2 V^{-1} s^{-1} for the In943 and In843 samples, respectively. This variation with the annealing temperature is consistent with the higher hole density measured in the In943 sample with respect to the In843 sample, corresponding to a higher concentration of In^{1+} vacancies and hence, enhanced point-defect scattering.

μ_H remains temperature independent between 5 and 175 K indicative of neutral impurity scattering. An exception to this behavior is the sample annealed at 943 K for which μ_H monotonically rises upon heating to 300 K, indicative of grain boundary scattering. The two other samples show a similar behavior above 175 K with a steep rise in μ_H, which also indicates that grain boundary scattering prevails up to 300 K. The significantly lower μ_H values of the Te943 sample that vary down to 1 cm^2 V^{-1} s^{-1} at low temperatures are likely due to microstructural effects, that is, the lower density of this sample and the presence of the precipitated secondary phase. The activated behavior observed for all samples annealed at the In-rich side are consistent with the presence of intrinsic resistance from grain boundaries that limits their electrical conductivity. The fact that this effect is strongly reduced in the In843 sample agrees with the higher μ_H values compared to the other samples and the strongly lessened activated behavior in $\rho(T)$. The data measured on the single-crystalline sample saturation-annealed at 893 K show that conventional acoustic phonon scattering prevails (Figure S10 in SI), demonstrating that grain boundaries govern the temperature dependence of μ_H in InTe. The comparison with the data reported previously on the as-grown single crystal of InTe reveals that the saturation annealing process leads to a significant improvement in the hole mobility.

Figure 4a shows the temperature dependence of the thermopower α. The α values remain positive for all the samples down to 5 K indicating a p-type electrical conduction, in agreement with the sign of R_H and with prior reports on single-crystalline and polycrystalline InTe.[46-60] Below 50 K, $\alpha(T)$ shows a weak but discernible maximum near 20 K, suggestive of a phonon-drag contribution, as observed in SnTe for instance.[69] For all samples, $\alpha(T)$ increases with increasing temperature up to about 650 K reflecting their degenerate character. Above this temperature, $\alpha(T)$ reaches a maximum before decreasing upon further heating. This variation signals excitation of electrons across the band gap E_g that can be estimated using the Goldsmid-Sharp relation $E_g = 2e\alpha_{max}T_{max}$ where e is the elemental charge.[70] Using $\alpha_{max} \approx 225$ µV K^{-1} reached at $T_{max} \approx 725$ K yields $E_g \approx 0.33$ eV. This value is in fair agreement with those inferred from absorption spectroscopy on Cd-doped samples and for single-crystalline InTe and polycrystalline Pb-doped samples.[53,55,56] The α values decrease with increasing the annealing temperature, reflecting the increase in p_H. The absence of significant anisotropy in α between the parallel and perpendicular directions below 650 K (see Figure S6 in SI) is explained by the nearly-parabolic valence band that gives rise to weakly-anisotropic ellipsoidal hole pockets forming the Fermi surface of lightly-doped p-type InTe.[54,58]

Due to the high ρ values, the power factors $P = \alpha^2/\rho$ remain moderate in the entire temperature range (Figure 4b). The P values are in good agreement with those measured in single-crystalline InTe,[55] with an optimum value of 0.51 mW m^{-1} K^{-2} achieved at 660 K in InTe. The decrease in the α values due to the increased hole concentrations in the saturation-annealed samples is responsible for the lowered P values, with a peak of 0.47 mW m^{-1} K^{-2} achieved at ~ 665 K for the In893 sample.

The $\alpha(p_H)$ dependence (Figure 5) at 300 K is consistent with the theoretical curve calculated using a single-parabolic-band (SPB) model. All the samples fall on the curve corresponding to a density-of-states effective mass of $0.74m_e$, indicating that varying the defect concentration likely corresponds to a mere rigid shift of the chemical potential deeper inside the valence bands.

Figure 6a shows the temperature dependence of total thermal conductivity κ. Below 300 K, all samples behave as typical crystalline compounds, with an Umklapp peak near 18 K in agreement with prior studies on InTe.[55,57,58] Comparatively, the temperature at which this maximum is reached is higher than in single-crystalline InTe.[55,57] This difference stems from grain boundary scattering that affects both the magnitude and temperature of this peak. The significantly lower peak observed in the In943 sample is consistent with the strongly reduced hole mobility indicative of enhanced point-defect scattering that dominates the charge and thermal transport in this sample. The extremely low κ values measured in the Te943 sample are mostly due to the low density of this sample. Upon warming, κ monotonically decreases to reach values as low as ~ 0.4 W m^{-1} K^{-1} at 800 K. The saturation annealing process has little influence on κ with only slight differences observed above 300 K that disappear at high temperatures. The lattice thermal conductivity κ_{ph} has been determined by subtracting the electronic contribution κ_e calculated using the Wiedemann-Franz law $\kappa_e = LT/\rho$ where L is the Lorenz number. The temperature dependence of L has been estimated using the SPB model. Regardless of the annealing temperature, κ_{ph} decreases with increasing temperature to reach ~ 0.25 W m^{-1} K^{-1} at 800 K (Figure 6b). These extremely low κ_{ph} values have been shown to originate from the disordered, rattling-like In$^+$ cations.[54,57] Associated with the thermal motion of these cations are low-energy optical modes that shape the low-energy region of the phonon spectrum.[54] By strongly limiting the phase space of acoustic phonons, these modes significantly lower κ_{ph}.

The temperature dependence of ZT is shown in Figure 7. The combination of high power factors and very low κ values results in high ZT values of up to 0.9 at 710 K for the InTe sample. The increased hole concentration induced by the saturation annealing process leads to reduced, yet still high ZT values ranging between 0.7 and 0.8 at 770 K. These values are similar to those reported for single-crystalline InTe, but remain lower than those achieved by alloying with Pb with a peak *ZT* of 1.05 at 780 K.[55,56]

3. CONCLUSION

To control the defect chemistry in InTe, polycrystalline and single-crystalline samples were subjected to saturation annealing on the In-rich and Te-rich sides of the solidus line at temperatures varying between 843 and 943 K. The concentration of In vacancies was effectively modified, with hole concentrations increasing from 4.9×10^{19} to 8.5×10^{19} cm^{-3} at 300 K upon increasing the annealing temperature. The resulting enhanced degenerate character of the annealed samples tends to lower the power factor and hence, the *ZT* values compared to as-synthesized InTe that exhibits the highest thermoelectric performance with a peak *ZT* value of ~ 0.9 at 710 K. Further first-principles defect calculations would be an interesting undertaking to devise effective doping strategies for either increasing the hole concentration or possibly achieving *n*-type electrical conduction.

ASSOCIATED CONTENT

The Supporting Information is available free of charge at https://pubs.acs.org/doi/

> Experimental section, photograph of the silica boat used for the saturation annealing process, elemental X-ray mappings of the as-synthesized and saturation-annealed samples, SEM image of the microstructure of a polycrystalline InTe sample, comparison of transport properties measurements performed parallel and perpendicular to the pressing direction, low-temperature dependence of the electrical resistivity and Hall mobility measured on the single-crystalline (SC) InTe sample saturation-annealed (SA) on the In-rich side at 893 K (In893) (PDF)

AUTHOR INFORMATION

Corresponding Authors

Christophe Candolfi – *Institut Jean Lamour, UMR 7198 CNRS – Université de Lorraine, Campus ARTEM, 2 allée André Guinier, BP 50840, 54011 Nancy, France*; orcid.org/0000-0002-1248-5354; Email: christophe.candolfi@univ-lorraine.fr

Bertrand Lenoir – *Institut Jean Lamour, UMR 7198 CNRS – Université de Lorraine, Campus ARTEM, 2 allée André Guinier, BP 50840, 54011 Nancy, France*; orcid.org/0000-0001-9631-4925; Email: bertrand.lenoir@univ-lorraine.fr

Authors

Shantanu Misra – *Institut Jean Lamour, UMR 7198 CNRS – Université de Lorraine, Campus ARTEM, 2 allée André Guinier, BP 50840, 54011 Nancy, France*; orcid.org/0000-0003-3419-4096; Email: shantanu_mi@yahoo.com

Petr Levinský – *FZU – Institute of Physics of the Czech Academy of Sciences, Cukrovarnická 10/112, 162 00, Prague 6, Czech Republic*; orcid.org/0000-0002-8501-1256; Email: levinsky@fzu.cz

Jiří Hejtmánek – *FZU – Institute of Physics of the Czech Academy of Sciences, Cukrovarnická 10/112, 162 00, Prague 6, Czech Republic*; orcid.org/0000-0001-8248-3912; Email: hejtman@fzu.cz

Author contributions

C.C. and B.L. designed, directed and supervised the study. S.M. synthesized the single-crystalline and polycrystalline samples, performed sample characterizations by PXRD and SEM and measured high-temperature thermal diffusivity. P.L., J.H, C.C. and B.L. performed the low- and high-temperature transport properties measurements. S.M. wrote the first draft of the manuscript. All authors proofread and corrected the manuscript and have given approval to its final version.

Notes

The authors declare no competing financial interest.

ACKNOWLEDGMENTS

P. L. and J. H. acknowledge the financial support of the Operational Program Research, Development and Education financed by European Structural and Investment Funds and the Czech Ministry of Education, Youth and Sports (Project No. SOLID21 CZ.02.1.01/0.0/0.0/16_019/0000760). Experiments were performed in MGML (mgml.eu), which is supported within the program of Czech Research Infrastructures (project no. LM2018096).

REFERENCES

(1) Goldsmid, H. J. in *Thermoelectric Refrigeration*, Springer, New York, USA, **1964**.

(2) Rowe, D. M. in *Thermoelectrics and its Energy Harvesting*, CRC Press, Boca Raton, FL, **2012**.

(3) Bell, L. E. Cooling, Heating, Generating Power, and Recovering Waste Heat with Thermoelectric Systems. *Science* **2008**, *321*, 1457–1461.

(4) Pei, Y.; Shi, X.; LaLonde, A.; Wang, H.; Chen L.; Snyder, G. J. Convergence of Electronic Bands for High Performance Bulk Thermoelectrics. *Nature* **2011**, *473,* 66–69.

(5) Zhang, J.; Liu, R.; Cheng, N.; Zhang, Y.; Yang, J.; Uher, C.; Shi, X.; Chen L.; Zhang, W. High-performance Pseudocubic Thermoelectric Materials from Non-Cubic Chalcopyrite Compounds. *Adv. Mater.* **2014**, *26*, 3848–3853.

(6) Heremans, J. P.; Wiendlocha, B.; Chamoire, A. M. Resonant Levels in Bulk Thermoelectric Semiconductors. *Energy Environ. Sci.* **2012**, *5*, 5510–5530.

(7) Heremans, J. P.; Jovovic, V.; Toberer, E. S.; Saramat, A.; Kurosaki, K.; Charoenphakdee, A.; Yamanaka, S.; Snyder, G. J. Enhancement of Thermoelectric Efficiency in PbTe by Distortion of the Electronic Density of States. *Science* **2008**, *321*, 554–557.

(8) Jaworski, C. M.; Kulbachinskii, V.; Heremans, J. P. Resonant Level Formed by Tin in Bi_2Te_3 and the Enhancement of Room-Temperature Thermoelectric Power. *Phys. Rev. B* **2009**, *80*, No. 233201.

(9) Wojciechowski, K. T.; Parashchuk, T.; Wiendlocha, B.; Cherniushok, O.; Dashevsky, Z. Highly Efficient *n*-type PbTe Developed by Advanced Electronic Structure Engineering. *J. Mater. Chem. C* **2020**, *8,* 13270–13285.

(10) Kriener, M.; Sakano, M.; Kamitani, M.; Bahramy, M. S.; Yukawa, R.; Horiba, K.; Kumigashira, H.; Ishizaka, K.; Tokura, Y.; Taguchi, Y. Evolution of Electronic States and

Emergence of Superconductivity in the Polar Semiconductor GeTe by Doping Valence-Skipping Indium. *Phys. Rev. Lett.* **2020**, *124*, No. 047002.

(11) Wiendlocha, B.; Misra, S.; Dauscher, A.; Lenoir, B.; Candolfi, C. Residual Resistivity as an Independent Indicator of Resonant Levels in Semiconductors. *Mater. Horiz.* **2021**, *8*, 1735–1743.

(12) Misra, S.; Wiendlocha, B.; Tobola, J.; Fesquet, F.; Dauscher, A.; Lenoir, B.; Candolfi, C. Band Structure Engineering in $Sn_{1.03}Te$ Through an In-Induced Resonant Level. *J. Mater. Chem. C* **2020**, *8*, 977–988.

(13) Wiendlocha, B.; Vaney, J.-B.; Candolfi, C.; Dauscher, A.; Lenoir, B.; Tobola, J. An Sn-Induced Resonant Level in β-As_2Te_3. *Phys. Chem. Chem. Phys.* **2018**, *20*, 12948–12957.

(14) Zhang, Q.; Wang, H.; Liu, W.; Wang, H.; Yu, B.; Zhang, Q.; Tian, Z.; Ni, G.; Lee, S.; Esfarjani, K.; Chen, G.; Ren, Z. Enhancement of Thermoelectric Figure-of-Merit by Resonant States of Aluminium Doping in Lead Selenide. *Energy Environ. Sci.* **2012**, *5*, 5246–5251.

(15) Vaney, J.-B.; Aminorroaya Yamini, S.; Takaki, H.; Kobayashi, K.; Kobayashi, N.; Mori, T. Magnetism-Mediated Thermoelectric Performance of the Cr-doped Bismuth Telluride Tetradymite. *Mater. Today Phys.* **2019**, *9*, No. 100090.

(16) Tan, G.; Zhao, L.-D.; Kanatzidis, M. G. Rationally Designing High-Performance Bulk Thermoelectric Materials. *Chem. Rev.* **2016**, *116*, 12123–12149.

(17) Lu, X.; Morelli, D. T.; Xia, Y.; Zhou, F.; Ozolins, V.; Chi, H.; Zhou, X.; Uher, C. High Performance Thermoelectricity in Earth-Abundant Compounds Based on Natural Mineral Tetrahedrites. *Adv. Energy Mater.* **2012**, *3*, 342–348.

(18) Tamaki, H.; Sato, H. K.; Kanno, T. Isotropic Conduction Network and Defect Chemistry in $Mg_{3+\delta}Sb_2$-Based Layered Zintl Compounds with High Thermoelectric Performance. *Adv. Mater.* **2016**, *28*, 10182–10187.

(19) Dong, Y.; Khabibullin, A. R.; Wei, K.; Salvador, J. R.; Nolas, G. S.; Woods, L. M. Bournonite $PbCuSbS_3$: Stereochemically Active Lone-Pair Electrons that Induce Low Thermal Conductivity. *Chem. Phys. Chem.* **2015**, *16*, 3264–3270.

(20) Fu, T.; Yue, X.; Wu, H.; Fu, C.; Zhu, T.; Liu, X.; Hu, L.; Ying, P.; He, J.; Zhao, X. Enhanced Thermoelectric Performance of PbTe Bulk Materials with Figure of Merit zT >2 by Multi-Functional Alloying. *J. Materiomics* **2016**, *2,* 141–149.

(21) Jood, P.; Ohta, M.; Yamamoto, A.; Kanatzidis, M. G. Excessively Doped PbTe with Ge-Induced Nanostructures Enables High-Efficiency Thermoelectric Modules. *Joule* **2018**, *2,* 1339–1355.

(22) Biswas, K.; He, J.; Zhang, Q.; Wang, G.; Uher, C.; Dravid, V. P.; Kanatzidis, M. G. Strained Endotaxial Nanostructures with High Thermoelectric Figure of Merit. *Nat. Chem.* **2011**, *3*, 160–166.

(23) Yu, Y.; Cagnoni, M.; Cojocaru-Mirédin, O.; Wuttig, M. Chalcogenide Thermoelectrics Empowered by an Unconventional Bonding Mechanism. *Adv. Funct. Mater.* **2020**, *30,* No. 1904862.

(24) Woods-Robinson, R.; Han, Y.; Zhang, H.; Ablekim, T.; Khan, I.; Persson, K. A.; Kutayev, A. Wide Band Gap Chalcogenide Semiconductors. *Chem. Rev.* **2020**, *120*, 4007–4055.

(25) Dennler, G.; Chmielowski, R.; Jacob, S.; Capet, F.; Roussel, P.; Zastrow, S.; Nielsch, K.; Opahle, I.; Madsen, G. K. H. Are Binary Copper Sulfides/Selenides Really New and Promising Thermoelectric Materials? *Adv. Energy Mater.* **2014**, *4,* No. 1301581.

(26) Guélou, G.; Lemoine, P.; Raveau, B.; Guilmeau, E. Recent Developments in High-Performance Thermoelectric Sulphides: an Overview of the Promising Synthetic Colusites. *J. Mater. Chem. C* **2021**, *9,* 773–795.

(27) Gougeon, P.; Gall, P.; Merdrignac-Conanec, O.; Aranda, L.; Dauscher, A.; Candolfi, C.; Lenoir, B. Synthesis, Crystal Structure, and Transport Properties of the Hexagonal Mo_9 Cluster Compound $Ag_3RbMo_9Se_{11}$. *Inorg. Chem.* 2017, **56**, 9684–9692.

(28) Vaney, J.-B.; Carreaud, J.; Delaizir, G.; Piarristeguy, A.; Pradel, A.; Alleno, E.; Monnier, J.; Lopes, E. B.; Gonçalves, A. P.; Dauscher, A.; Candolfi, C.; Lenoir, B. High Thermoelectric Performance in Sn-Substituted α-As_2Te_3. *J. Mater. Chem. C* **2016**, *4*, 2329–2338.

(29) Guo, Q.; Chan, M.; Kuropatwa, B. A.; Kleinke, H. Enhanced Thermoelectric Properties of Variants of Tl_9SbTe_6 and Tl_9BiTe_6. *Chem. Mater.* **2013**, *25*, 4097–4104.

(30) Tanimoto, T.; Suekuni, K.; Tanishita, T.; Usui, H.; Tadano, T.; Komei, T.; Saito, H.; Nishiate, H.; Lee, C. H; Kuroki, K.; Ohtaki, M. Enargite Cu_3PS_4: A Cu–S-Based Thermoelectric Material with a Wurtzite-Derivative Structure. *Adv. Funct. Mater.* **2020**, *30*, No. 2000973.

(31) Qiu, P.; Zhang, T.; Qiu, Y.; Shi, X.; Chen, L. Sulfide Bornite Thermoelectric Material: a Natural Mineral with Ultralow Thermal Conductivity. *Energy Environ. Sci.* **2014**, *7*, 4000–4006.

(32) Tang, Y.; Hanus, R.; Chen, S.-W.; Snyder, G. J. Solubility Design Leading to High Figure of Merit in Low-Cost Ce-$CoSb_3$ Skutterudites. *Nat. Commun.* **2015**, *6*, No. 7584.

(33) Ohno, S.; Aydemir, U.; Amsler, M.; Pöhls, J.-H.; Chanakian, S.; Zevalkink, A.; White, M. A.; Bux, S. K.; Wolverton, C.; Snyder, G. J. Achieving zT > 1 in Inexpensive Zintl Phase $Ca_9Zn_{4+x}Sb_9$ by Phase Boundary Mapping. *Adv. Funct. Mater.* **2017**, *27*, No. 1606361.

(34) Imasato, K.; Fu, C.; Pan, Y.; Wood, M.; Kuo, J. J.; Felser, C.; Snyder, G. J. Metallic *n*-type Mg_3Sb_2 Single Crystals Demonstrate the Absence of Ionized Impurity Scattering and Enhanced Thermoelectric Performance. *Adv. Mater.* **2020**, *32*, No. 1908218.

(35) McHugh, J. P.; Tiller, W. A. The Germanium-Tellurium Phase Diagram in the Vicinity of the Compound GeTe. *Trans. Met. Soc. AIME* **1960**, *218*, 187–188.

(36) Brebrick, R. F.; Gubner, E. Composition Stability Limits of PbTe. II. *J. Chem. Phys.* **1962**, *36*, 1283–1289.

(37) Bloem, J.; Kroger, F. A. The *p-T-x*-phase Diagram of the Lead-Sulphur System. *Z. Phys. Chem.* **1956**, *7*, 1–14.

(38) Hewes, C.; Adler, M. S.; Senturia, S. D. Annealing Studies of PbTe and $Pb_{1-x}Sn_xTe$. *J. Appl. Phys.* **1973**, *44*, 1327–1332.

(39) Fleurial, J. P.; Gailliard, L.; Triboulet, R.; Scherrer, H.; Scherrer, S. Thermal Properties of High Quality Single Crystals of Bismuth Telluride—Part I: Experimental Characterization. *J. Phys. Chem. Solids* **1988**, *49*, 1237–1247.

(40) Fleurial, J. P.; Gailliard, L.; Triboulet, R.; Scherrer, H.; Scherrer, S. Thermal Properties of High Quality Single Crystals of Bismuth Telluride—Part II: Mixed-Scattering Model. *J. Phys. Chem. Solids* **1988**, *49*, 1249–1257.

(41) Brebrick, R. F. Homogeneity Ranges and Te_2-Pressure along the Three-Phase Curves for Bi_2Te_3(c) and a 55–58 at.% Te Peritectic Phase. *J. Phys. Chem. Solids* **1969**, *30*, 719–731.

(42) Brebrick, R. F. Analysis of the Solidus Lines for PbTe and SnTe. *J. Electron. Mater.* **1977**, *6*, 659–692.

(43) Brebrick, R. F. Composition Stability Limits of Binary Semiconductor Compounds. *J. Phys. Chem. Solids* **1961**, *18*, 116–128.

(44) Ibrahim, D.; Misra, S.; Migot, S.; Ghanbaja, J.; Dauscher, A.; Malaman, B.; Semprimoschnig, C.; Candolfi, C; Lenoir, B. Transport Properties of Polycrystalline SnTe Prepared by Saturation Annealing. *RSC Advances* **2020**, *10*, 5996–6005.

(45) Albers, W.; Haas, C.; Vink, H. J.; Wasscher, J. D. Investigations on SnS. *J. Appl. Phys.* **1961**, *32*, 2220–2225.

(46) Jana, M. K.; Pal, K.; Waghmare, U. V.; Biswas, K. The Origin of Ultralow Thermal Conductivity in InTe: Lone-Pair-Induced Anharmonic Rattling. *Angew. Chem.* **2016**, *55*, 7792–7796.

(47) Back, S. Y.; Cho, H.; Kim, Y. K.; Byeon, S.; Jin, H.; Koumoto, K.; Rhyee, J. S. Enhancement of Thermoelectric Properties by Lattice Softening and Energy Band Gap Control in Te-Deficient $InTe_{1-\delta}$. *AIP Adv.* **2018**, *8*, No. 115227.

(48) Zhu, H.; Zhang, B.; Wang, G.; Peng, K.; Yan, Y.; Zhang, Q.; Han, X.; Wang, G.; Lu, X.; Zhou, X. Promoted High Temperature Carrier Mobility and Thermoelectric Performance of InTe Enabled by Altering Scattering Mechanism. *J. Mater. Chem. A* **2019**, *7*, 11690–11698.

(49) Chattopadhyay, T.; Santandrea, R. P.; von Schnering, H. G. Temperature and Pressure Dependence of the Crystal Structure of InTe: A New High Pressure Phase of InTe. *J. Phys. Chem. Solids* **1985**, *46*, 351–356.

(50) Pal, S.; Bose, D. N. Growth, Characterisation and Electrical Anisotropy in Layered Chalcogenides GaTe and InTe. *Solid State Commun.* **1996**, *97*, 725–729.

(51) Nizametdinova, M. A. Raman Spectrum of InTe and TlSe Single Crystals. *Phys. Status Solidi B* **1980**, *97*, K9–K12.

(52) Rajaji, V.; Pal, K.; Ch. Sarma, S.; Joseph, B.; Peter, S. C.; Waghmare, U. V.; Narayana, C. Pressure Induced Band Inversion, Electronic and Structural Phase Transitions in InTe: A Combined Experimental and Theoretical Study. *Phys. Rev. B* **2018**, *97*, No. 155158.

(53) Pan, S.; Liu, H.; Li, Z.; You, L.; Dai, S.; Yang, J.; Guo, K.; Luo, J. Enhancement of the Thermoelectric Performance of InTe via Introducing Cd Dopant and Regulating the Annealing Time. *J. Alloys Compd.* **2020**, *813*, No. 152210.

(54) Misra, S.; Barreteau, C.; Crivello, J.-C.; Giordano, V. M.; Castellan, J.; Sidis, Y.; Levinsky, P.; Hejtmánek, J.; Malaman, B.; Dauscher, A.; Lenoir, B.; Candolfi, C.; Pailhès, S. Reduced

Phase Space of Heat-Carrying Acoustic Phonons in Single-Crystalline InTe. *Phys. Rev. Res.* **2020**, *2*, No. 043371.

(55) Misra, S.; Levinsky, P.; Dauscher, A.; Medjahdi, G.; Hejtmánek, J.; Malaman, B.; Snyder, G. J.; Lenoir, B.; Candolfi, C. Synthesis and Physical Properties of Single-Crystalline InTe: Towards High Thermoelectric Performance. *J. Mater. Chem. C* **2021**, *9*, 5250–5260.

(56) Misra, S.; Léon, A.; Levinsky, P.; Hejtmánek, J.; Lenoir, B.; Candolfi, C. Enhanced Thermoelectric Performance of InTe Through Pb Doping. *J. Mater. Chem. C* **2021**, *9*, 14490–14496.

(57) Zhang, J.; Roth, N.; Tolborg, K.; Takahashi, S.; Song, L.; Bondesgaard, M.; Nishibori, E.; Iversen, B. B. Direct Observation of One-Dimensional Disordered Diffusion Channel in a Chain-like Thermoelectric with Ultralow Thermal Conductivity. *Nat. Commun.* **2021**, *12*, No. 6709.

(58) Back, S. Y.; Kim, Y. K.; Cho, H.; Han, M. K.; Kim, S. J.; Rhyee, J. S. Temperature-Induced Lifshitz Transition and Charge Density Wave in $InTe_{1-\delta}$ Thermoelectric Materials. *ACS Appl. Energy Mater.* **2020**, *3*, 3628–3636.

(59) Hussein, S. A. Temperature Dependences of the Electrical Conductivity and Hall Coefficient of Indium Telluride Single Crystals. *Cryst. Res. Tech.* **1989**, *24*, 635–638.

(60) Hogg, J. H. C.; Sutherland, H. H. Indium Telluride. *Acta Crystallogr. B* **1976**, *32*, 2689–2690.

(61) Belotskii, D. P.; Babyuk, P. F. The In_2Te_3-Sb_2Te_3 System. *Inorg. Chem.* **1970**, *6*, 505−507.

(62) Scherrer, H.; Scherrer, S. in *CRC Handbook of thermoelectricity*, Chap. 19, edited by Rowe, D. M., CRC Press, Boca Raton, FL, **1995**.

(63) Schlieper, A.; Feutelais, Y.; Fries, S. G.; Legendre, B.; Blachnik, R. Thermodynamic Evaluation of the Germanium-Tellurium System. *Calphad* **1999**, *23*, 1–18.

(64) Scherrer, H.; Pineau, G.; Scherrer, S. Diffusion of ^{117}Sn in Tin Telluride. *Phys. Lett.* **1979**, *75*, 118–120.

(65) Scherrer, H.; Weber, S.; Scherrer, S. Diffusion of ^{125}Te in Tin Telluride. *Phys. Lett.* **1980**, *77*, 189–190.

(66) Parlak, M.; Erçelebi, C.; Günal, I.; Özkan, H.; Gasanly, N. M. Anisotropy of Electrical Resistivity and Hole Mobility in InTe Single Crystals. *Cryst. Res. Tech.* **1996**, *31*, 673–678.

(67) Riede, V.; Neumann, H.; Sobotta, H.; Lévy, F. Infrared Optical Properties of InTe. *Solid State Commun.* **1981**, *38*, 71–73.

(68) Goyal, A.; Gorai, P.; Toberer, E. S.; Stevanovic, V. First-Principles Calculation of Intrinsic Defect Chemistry and Self-Doping in PbTe. *npj Comput. Mater.* **2017**, *3*, No. 42.

(69) Ibrahim, D.; Candolfi, C.; Migot, S.; Ghanbaja, J.; Dauscher, A.; Le Caër, G.; Malaman, B.; Semprimoschnig, C.; Lenoir, B. Comprehensive Study of the Low-Temperature Transport Properties of Polycrystalline $Sn_{1+x}Te$ (x = 0 and 0.03). *Phys. Rev. Mater.* **2019**, *3*, No. 085404.

(70) Goldsmid, H. J.; Sharp, J. W. Estimation of the Thermal Band Gap of a Semiconductor from Seebeck Measurements. *J. Electron. Mater.* **1999**, *28*, 869–872.

Table caption

Table 1. Hole Densities p_H and Hall Mobilities μ_H Measured at 300 K for Non-Annealed and Saturation-Annealed InTe Samples. Experimental Uncertainty is Given in Parenthesis (see SI for further details).

Sample	p_H ($\times 10^{19}$ cm^{-3})	μ_H (cm^2 V^{-1} s^{-1})
InTe	4.4(0.2)	15.9(0.8)
In943	8.5(0.4)	9.0(0.4)
In893	7.6(0.4)	17.1(0.8)
In843	4.9(0.2)	18.4(0.9)
SC In893 (first)	9.5(0.5)	/
SC In893 (second)	11.8(0.6)	66.1(3.3)
Te943	5.2(0.3)	1.0(0.05)

Figure captions

Figure 1. Powder x-ray diffraction patterns for non-annealed and saturation-annealed InTe samples. Note that the anisotropic crystal structure of InTe tends to result in preferential orientation of the crystallites, explaining the differences observed in the relative intensity of the peaks from sample to sample.

Figure 2. Temperature dependence of the electrical resistivity ρ of the non-annealed and saturation-annealed InTe samples measured along the direction parallel to the pressing direction. The lines are guides to the eye.

Figure 3. Temperature dependence of the a) Hall coefficient R_H, b) hole concentration p_H, c) temperature of the saturation-annealing process as a function of p_H and d) Hall mobility μ_H of the non-annealed and saturation-annealed InTe samples measured along the direction parallel to the pressing direction. In panels a), b) and d), the solid lines are guides to the eye. In panel c), the dashed line represents the hypothetical solidus line. Note that the difference between the data of single-crystalline (SC) InTe and polycrystalline In-rich sample, all saturation-annealed at 893 K is due to the more pronounced anisotropy of the transport properties in the former. The direct comparison of data measured on single-crystalline and polycrystalline samples should be taken with some caution.

Figure 4. Temperature dependence of a) the thermopower α and b) the power factor P of the non-annealed and saturation-annealed InTe samples measured along the direction parallel to the pressing direction. The lines are guides to the eye.

Figure 5. Ioffe-Pisarenko plot at 300 K for non-annealed and saturation-annealed InTe samples measured along the direction parallel to the pressing direction. Data for single-crystalline InTe and from prior studies are also included for comparison (error bars corresponding to 7% have been included for both axes). The black solid and dashed lines were calculated using the SPB model with density-of-states effective masses m^*_{DOS} of $0.74m_e$ and $0.98m_e$, respectively.

Figure 6. Temperature dependence of a) total thermal conductivity κ and b) lattice thermal conductivity κ_{ph} for the non-annealed and saturation-annealed InTe samples measured along the direction parallel to the pressing direction. The lines are guides to the eye.

Figure 7. Dimensionless thermoelectric figure of merit ZT as a function of temperature for non-annealed and saturation-annealed samples along the direction parallel to the pressing direction. The lines are guides to the eye.

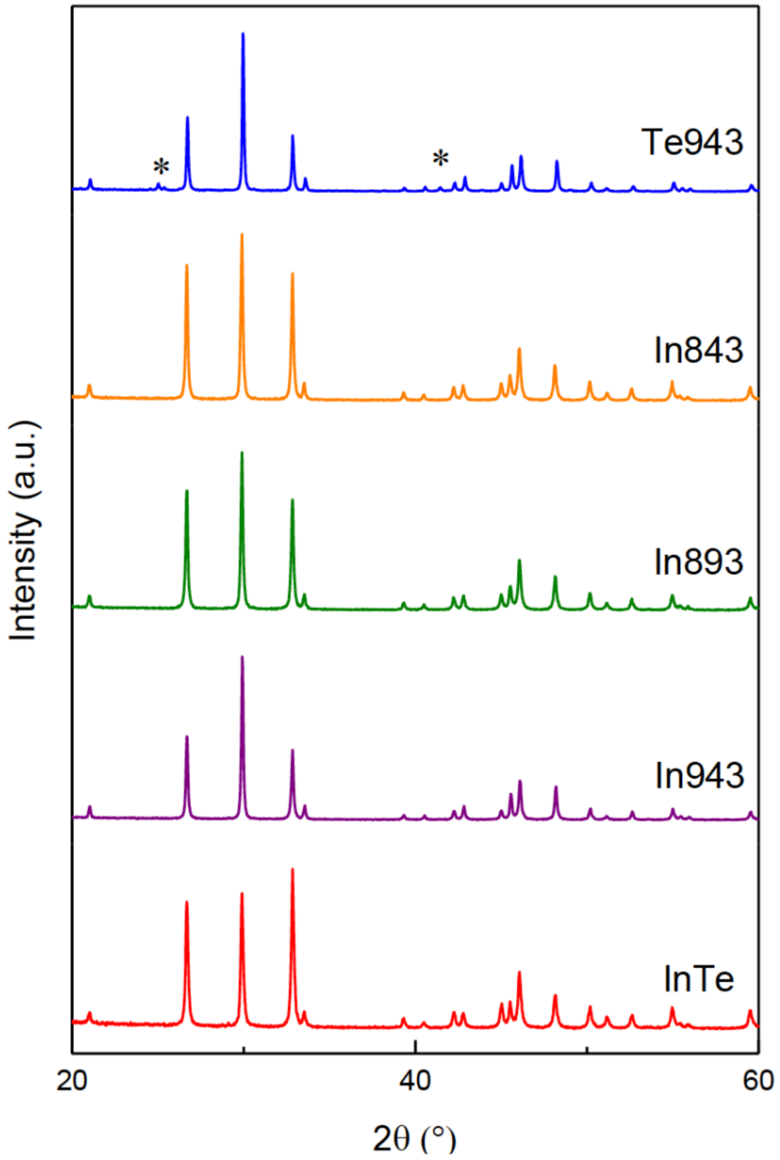

Figure 1

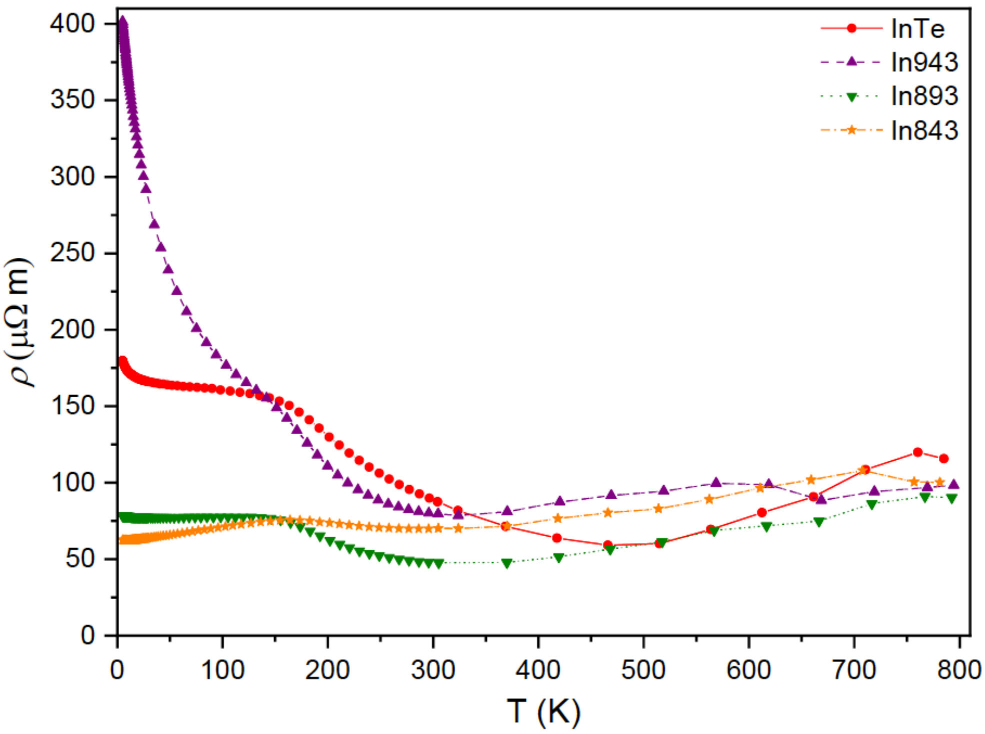
InTe
In943
In893
In843
ρ (μΩ m)
T (K)
0
50
100
150
200
250
300
350
400
0
100
200
300
400
500
600
700
800

Figure 2

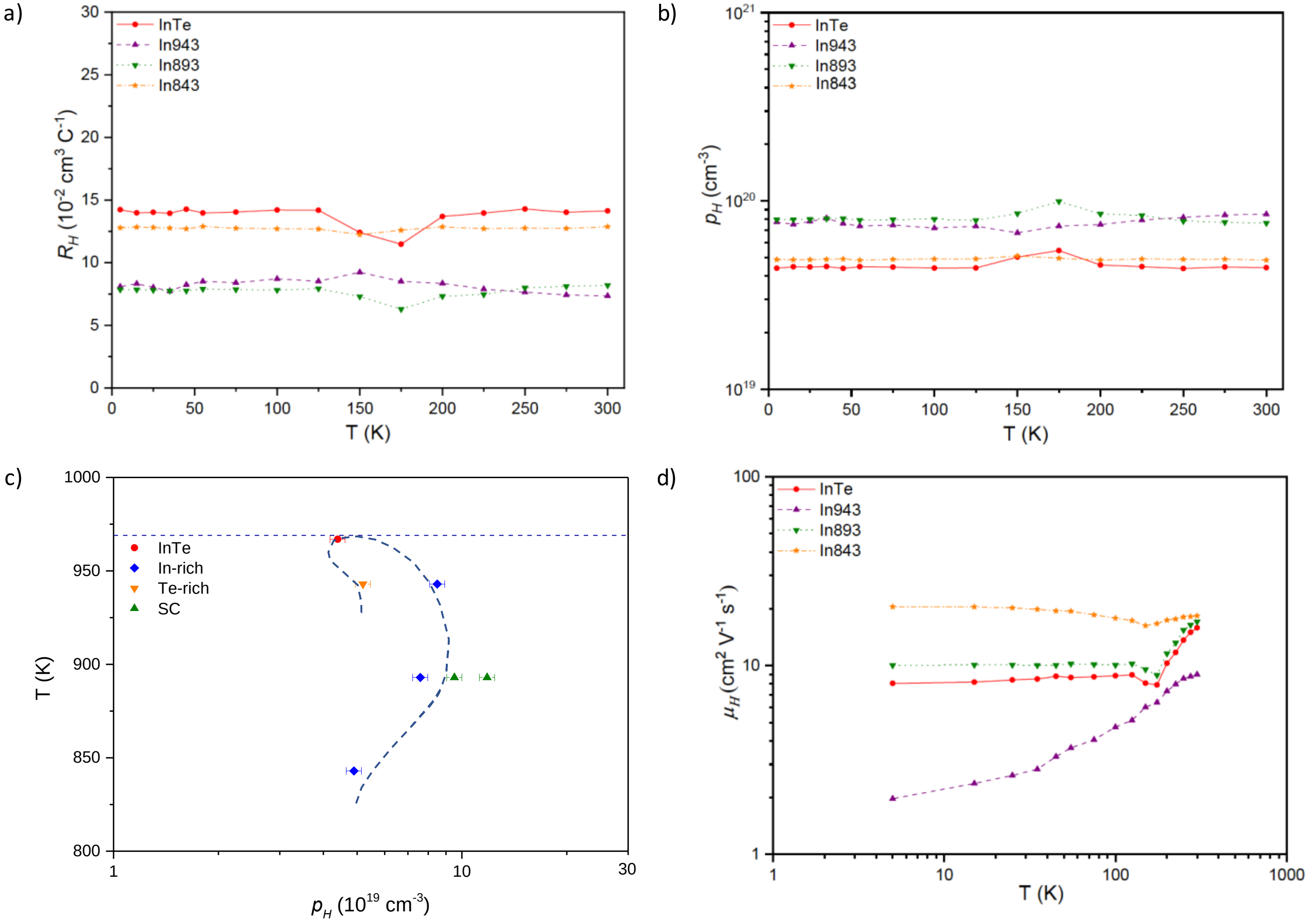
a)
R_H (10^{-2} cm^3 C^{-1})
T (K)
InTe
In943
In893
In843
0
5
10
15
20
25
30
0
50
100
150
200
250
300
b)
p_H (cm^{-3})
T (K)
InTe
In943
In893
In843
10^{19}
10^{20}
10^{21}
0
50
100
150
200
250
300
c)
T (K)
p_H (10^{19} cm^{-3})
InTe
In-rich
Te-rich
SC
800
850
900
950
1000
1
10
30
d)
μ_H(cm^2 V^{-1} s^{-1})
T (K)
InTe
In943
In893
In843
1
10
100
1
10
100
1000

Figure 3

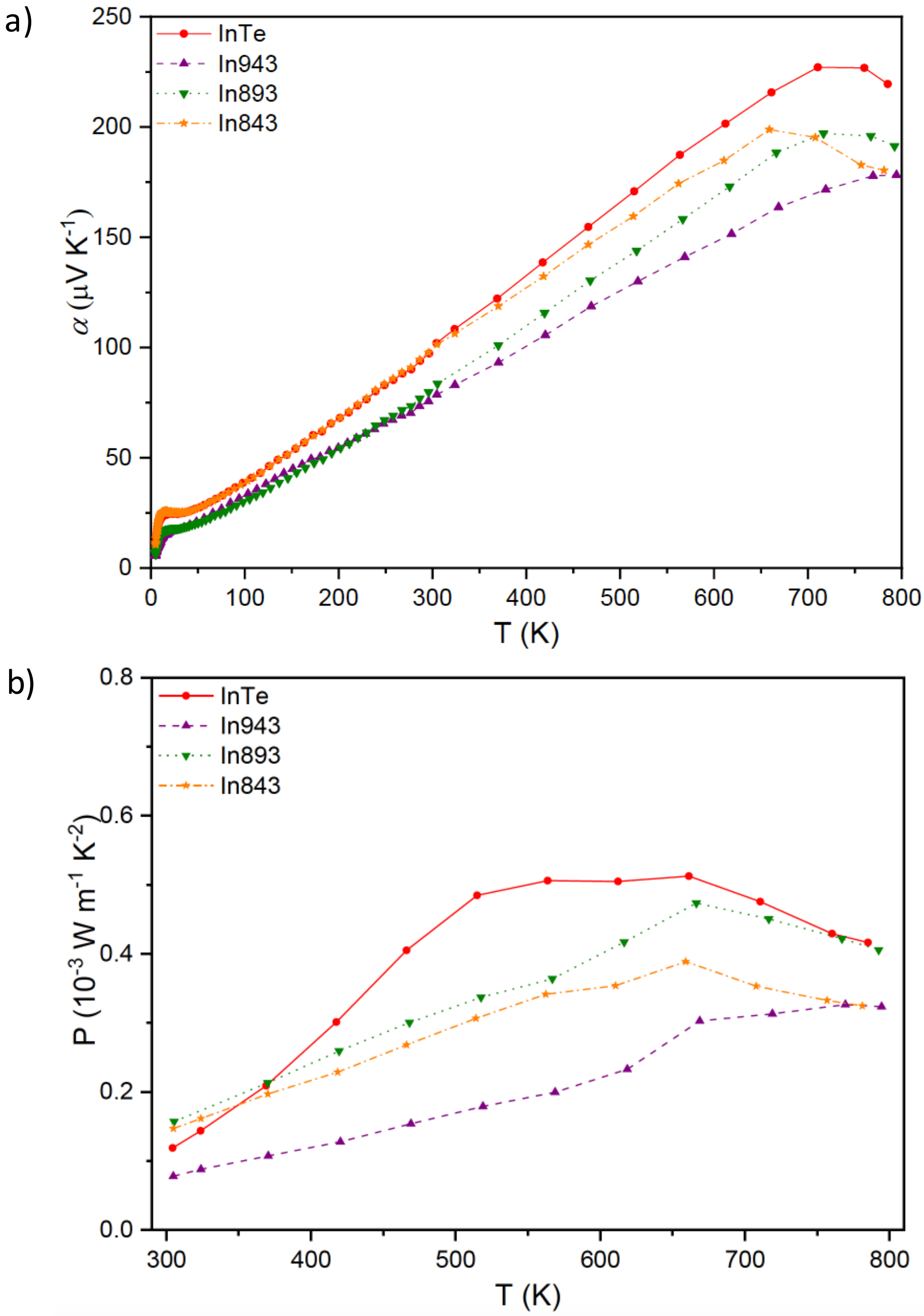
a)
250
200
150
100
50
0
α (μV K^{-1})
0
100
200
300
400
500
600
700
800
T (K)
InTe
In943
In893
In843
b)
0.8
0.6
0.4
0.2
0.0
P (10^{-3} W m^{-1} K^{-2})
300
400
500
600
700
800
T (K)
InTe
In943
In893
In843

Figure 4

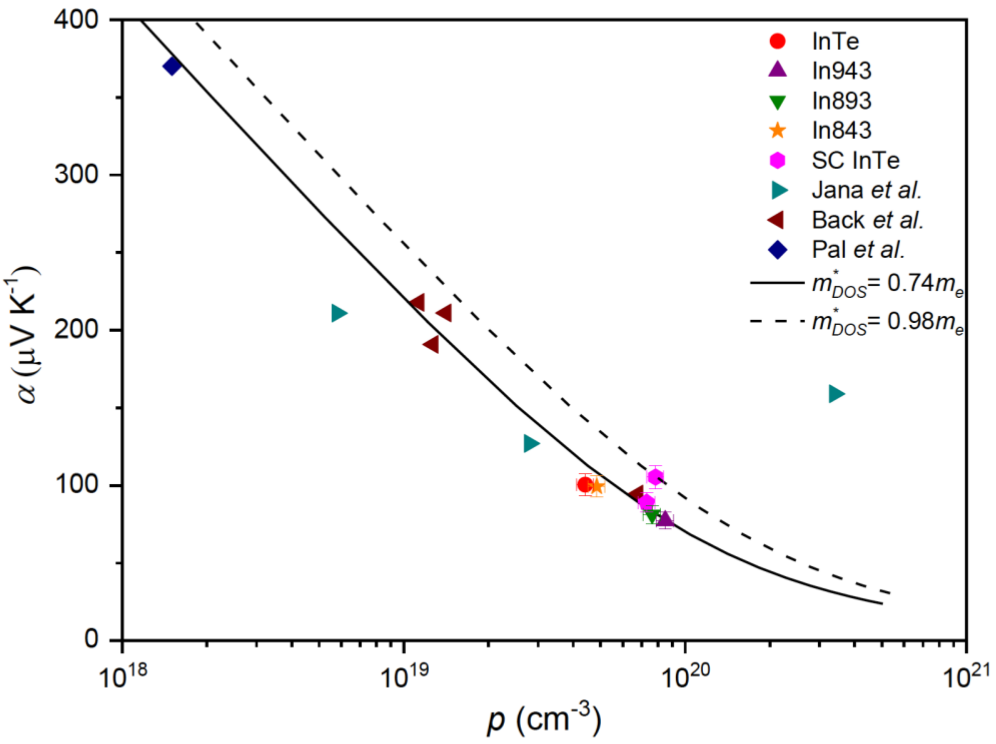

400
300
200
100
0
α (μV K^{-1})
10^{18}
10^{19}
10^{20}
10^{21}
p (cm^{-3})
InTe
In943
In893
In843
SC InTe
Jana *et al.*
Back *et al.*
Pal *et al.*
$m^*_{DOS} = 0.74m_e$
$m^*_{DOS} = 0.98m_e$

Figure 5

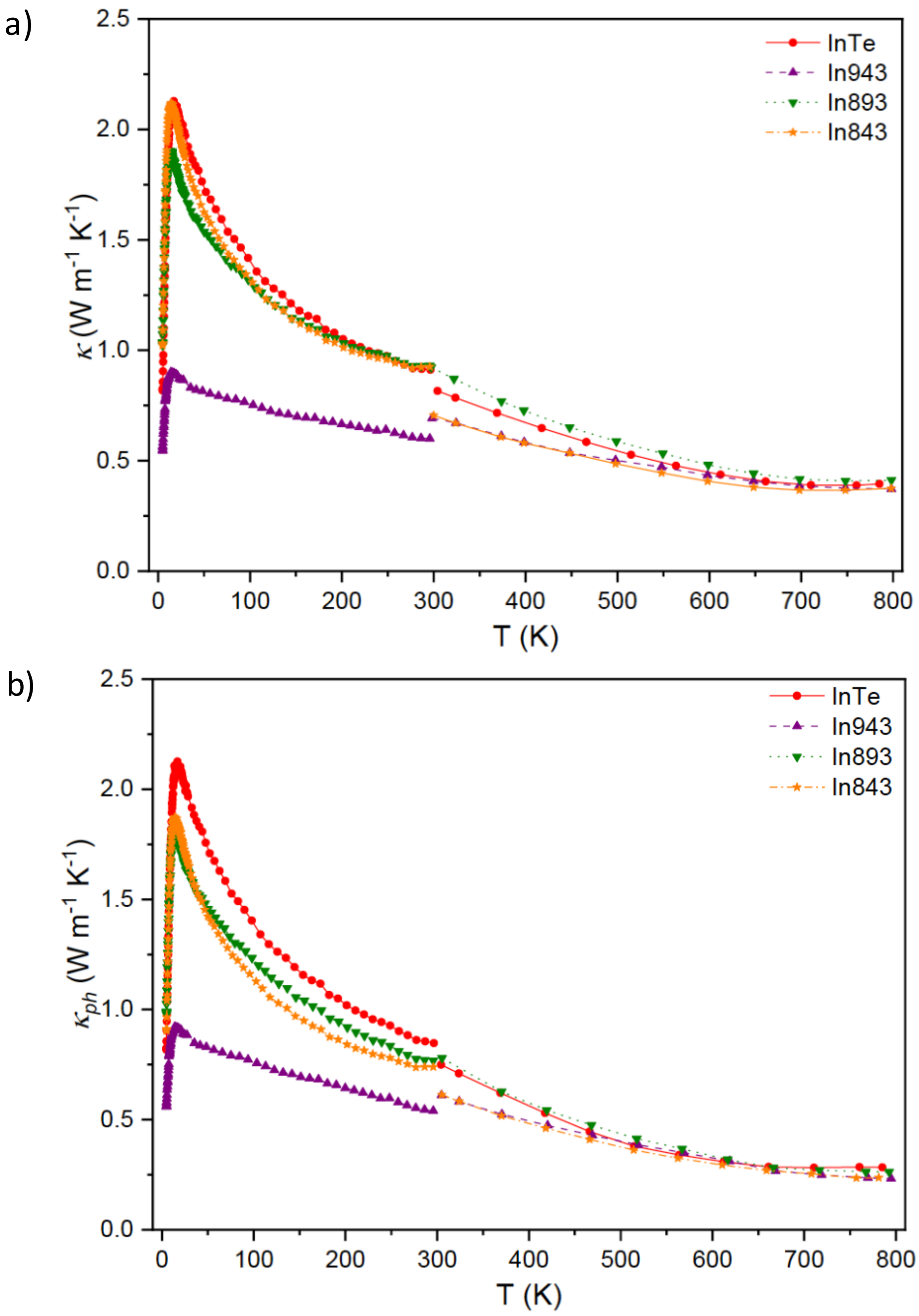
a)
κ (W m^{-1} K^{-1})
T (K)
InTe
In943
In893
In843
0.0
0.5
1.0
1.5
2.0
2.5
0
100
200
300
400
500
600
700
800
b)
κ_{ph} (W m^{-1} K^{-1})
T (K)
InTe
In943
In893
In843

Figure 6

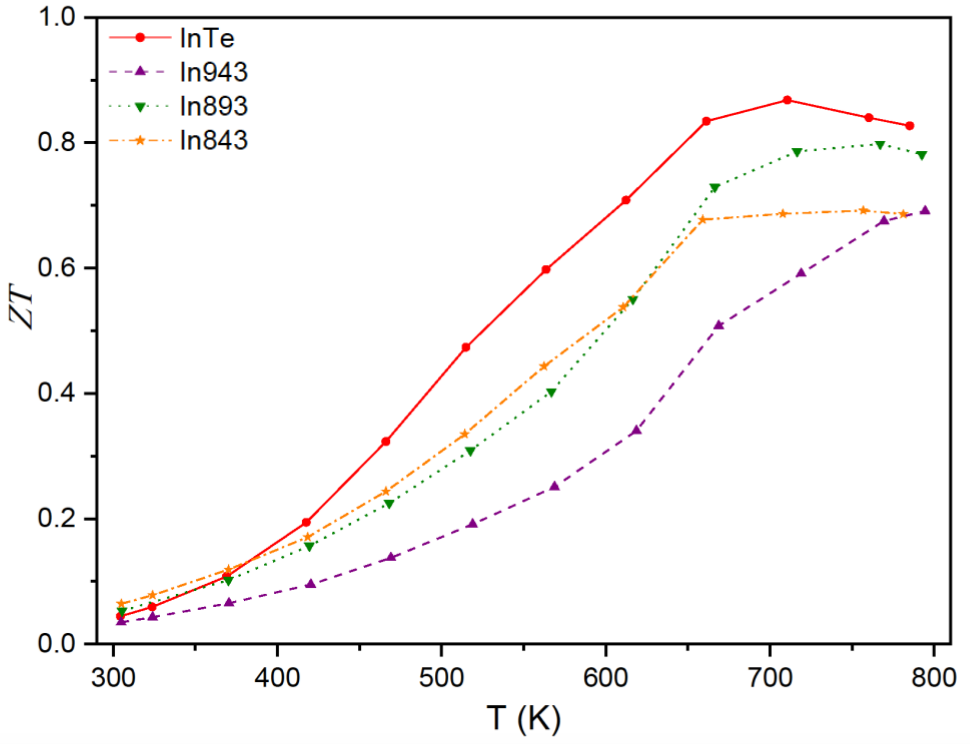
InTe
In943
In893
In843
1.0
0.8
0.6
0.4
0.2
0.0
ZT
300
400
500
600
700
800
T (K)

Figure 7

Table of Contents Graphic

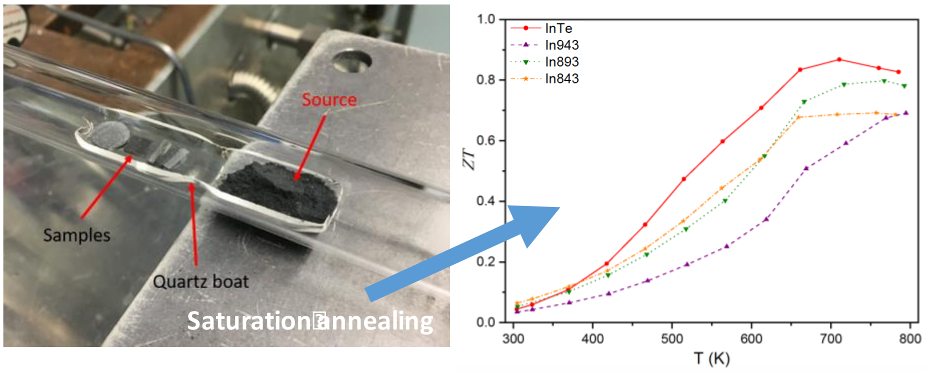

This work reports a detailed study of the saturation annealing process applied on single-crystalline and polycrystalline InTe on both the In-rich and Te-rich sides of the solidus line. This technique enables a precise control of the defect chemistry in chalcogenide semiconductors.